Article

JOURNAL OF THE CHINESE CHEMICAL SOCIETY

Synthesis and Photocatalytic Properties of Nano-crystalline In_2O_3

Yong-Ming Dai,[a] Wen-lian William Lee,[b,c] Wei-Chieh Lin[a] and Chiing-Chang Chen[a,*]

[a]*Department of Science Application and Dissemination, National Taichung University of Education, Taichung 403, Taiwan, ROC*

[b]*Department of Occupational Safety and Health, Chung-Shan Medical University, Taichung 402, Taiwan, ROC*

[c]*Department of Occupational Medicine, Chung Shan Medical University Hospital, Taichung, 40201 Taiwan, ROC*

(Received: Apr. 20, 2013; Accepted: Jul. 19, 2013; Published Online: Oct. 7, 2013; DOI: 10.1002/jccs.201300202)

A nano-crystalline In_2O_3 was synthesized using calcinations methods and was used as a photocatalyst to degrade sulfan blue (SB) dye. In addition, this study addresses the conditions of the degradation and the factors that influenced the catalysis. In_2O_3 was prepared by calcining $In(OH)_3$ at heat ranges of 100-700 ^oC for 24 h. The In_2O_3 was characterized using field emission scanning electron microscopy (FE-SEM), an X-ray diffractometer (XRD), thermogravimetric analysis (TGA), and high-resolution X-ray photoelectron spectroscopy (HR-XPS). The activities of these samples were tested for the photocatalytic degradation of SB dye. The results indicated that the $In(OH)_3$ that was calcined at 300 ^oC for 24 h had the best performance.

Keywords: Sulfan blue; Photodegradation; In_2O_3; Photocatalyst; Calcinations synthesis.

INTRODUCTION

The characteristics of dyes and dyeing wastewater include high temperature, high chromaticity, high pH, and high COD. The most frequently used dyeing wastewater treatment methods can be categorized as follows: biological treatment, physical adsorption, and chemical oxidation. Biological treatment technology chiefly uses bacteria, enzymes, or microorganisms to enable the dyes to decolorize.[1,2] However, in applied conditions, the high toxicity and concentration of dyeing wastewater restrains organisms' growth, making them ineffective in deconstructing dyes. Physical adsorption technology uses adsorbent materials with large surface areas, good chemical stability, and high resistance to microbial decomposition, such as active carbon, porcelain clay, alumina, red soil, and wollastonite,[3-6] to reduce the colorization of the dyeing wastewater. However, this method only transfers the adsorbed dyes elsewhere and does not remove dyes. Chemical oxidation technology uses strong oxidation effects to destroy the organic matter in the water, achieving decolorization, detoxification, and deodorization. This process has been examined by recent studies on dyeing wastewater treatment. The oxidation methods that can be used include ozone oxidation, chlorination oxidation, photooxidation, electrolysis oxidation, wet air oxidation, and advanced oxidation processes (AOPs). The advantage of using chemical oxidation technology and physical adsorption technology is their ability to breakdown dyes' organic pollutants quickly, and that they can treat high volumes or concentrations of dyeing wastewater.[7-9]

Photocatalytic technology is a wastewater treatment method that has been developed in the last 30 years. In 1972, Honda Fujishima found that using photocatalytic conductors to oxidize titanium single-crystal electrodes and white gold electrodes can directly photolyze water to form hydrogen. Thereafter, multiphase photocatalytic technology attracted worldwide interest.[10] In 1976, John H. Carry used photocatalytic technology in the dechlorination of PCBs and found that TiO_2 was suspended in the liquid. Following 30 min of light reaction, the chlorine with a concentration of 50 μg/L was completely dechlorinated and there was no chlorine in the intermediates.[11] In 1977, S. N. Frand used xenon lamps as his light source and found that TiO_2, ZnO, and CdS can effectively catalyze CN^- to CNO^-. Furthermore, TiO_2, ZnO, CdS, and Fe_2O_3 can effectively catalyze SO_3^{2-} to SO_4^{2-}.[12] Thereafter, studies on organic photocatalytic technology became common. In recent years, because studies on environmental waste control have become increasingly important, the photocatalytic oxidation method has been extensively used in studies regarding difficult organism decomposition in the air and water, demonstrating significant treatment effects.

* Corresponding author. Tel: +886-4-2218-3406; Fax: +886-4-2218-3560;
E-mail: ccchen@mail.ntcu.edu.tw; ccchen@ms3.ntcu.edu.tw

Photocatalytic oxidation is a high-level oxidation technology that uses sunlight as the radiation source to stimulate semiconductor catalysts (e.g., TiO_2, ZnO, CdS, and Fe_2O_3), producing electron-hole pairs that begin the redox reaction. For decomposing organic materials in wastewater, light produces electron holes and hydroxide radicals that have positive removal effects for organic substances in wastewater (e.g., hydrocarbon, halogenated organic compounds, carboxyl, surface active agents, herbicide, dyes, and organic matters with nitrogen) and inorganic substances (e.g., cyanogen ion, metallic ions). Following sustained reactions, making a substance inorganic is possible.[13-15]

In_2O_3 is an n-type semiconductor with a wide band gap (3.6 eV) that is used in solar batteries, lithium batteries, field emission displays, nano-bio sensors, gas sensors, optoelectronic devices, and photocatalysts.[16-22] In recent years, In_2O_3 has been used as a raw material for electro-optic modulators, electronic window heaters, electronic chrome mirrors, and nano-electronic substrate structures.[23-25] The crystal structure of In_2O_3 can be divided into two types: cubic crystal and hexagonal crystal. The structure of In_2O_3 is bixbyite with a lattice constant of 10.117 Å,[26,27] which belongs to the c-type rare earth group and has imperfect oxides. There are 16 groups of In_2O_3 in a single crystal cell, totaling 80 atoms. Bixbyite has a complicated and low-symmetry structure. The structure of the bixbyite of In_2O_3 is similar to that of fluorite MX_2 (e.g., CaF_2), although they differ in composition. One atom must be eliminated for every four oxygen atom. The two methods of the empty space encircling the indium atom are the b and d site, as determined by Wyckoff. For the b site, there are two openings for negative ions in the diagonal of the positive ion. The distance between the oxygen atom and negative ion is 2.18 Å. For the d site, there are two diagonal openings for ions. The distances between the oxygen ions in the deformed cube to the indium ion in the center are not equal: 2.13, 2.19, and 2.23 Å. Each cube is missing two oxygen ions, forming an octagonal structure InO_6 with In at its center. In_2O_3 has good electric conductivity and greater than 80% transmittance in the visible region. Therefore, it is frequently proposed in studies on transparent conductive films and organic photocatalysis.[28,29]

This study systematically investigated the controlled synthesis of nano-crystalline In_2O_3 using various calcinations methods and examined the effects of the influencing factors, including the initial concentrations of the dye and catalyst dosages. This study obtained a better understanding of the mechanistic details of the nano-crystalline In_2O_3-assisted photodegradation of the SB dye under UV irradiation.

EXPERIMENTAL

Materials. The experimental procedure was as follows. $In(OH)_3$ (99%, Aldrich) was placed in a high temperature chamber and was heated to 100-700 °C for 24 h and, thereafter, naturally cooled to room temperature. The sample preparation parameters are shown in Table 1.

Characterizations. The precipitates were further characterized. Powder X-ray diffraction (XRD) was performed with a MAC Sience MXP18 X-ray diffractometer with Cu Kα radiation and was performed at 40 kV and 80 mA. FE-SEM-EDS measurements were performed with a field-emission microscope (JEOL JSM-7401F) at an acceleration voltage of 15 kV, and an HRXPS

Table 1. Physical and chemical properties of the $In(OH)_3$ and prepared In_2O_3

Preparation condition			EDS element atomic ratio (%)		O/In (atomic ratio)	XPS element atomic ratio (%)		O/In (atomic ratio)	Eg (eV)
No.	Temp. (°C)	Time (hr)	In	O		In	O		
S100	100	24	10.65	89.35	8.39	24.84	62.93	2.53	-
S200	200	24	16.02	83.98	5.24	28.30	56.94	2.01	2.66
S300	300	24	25.93	74.07	2.86	34.76	54.00	1.55	2.64
S400	400	24	30.50	69.50	2.28	33.42	52.31	1.57	2.63
S500	500	24	21.47	78.53	3.66	29.94	49.25	1.64	2.59
S600	600	24	25.46	74.54	2.93	29.65	50.29	1.70	2.60
S700	700	24	19.65	80.35	4.09	27.83	51.57	1.85	2.54
	$In(OH)_3$		16.21	83.79	5.17	23.78	64.21	2.70	-
	In_2O_3		18.54	81.46	4.39	35.82	51.02	1.42	2.65

$$E_g = E = \frac{hc}{\lambda} = \frac{6.626068\times10^{-34}\times2.998\times10^{8}}{\lambda\times10^{-9}\times1.60217\times10^{-19}} = \frac{1240.2915}{\lambda}(eV)$$

measurement was carried out using ULVAC-PHI XPS. The Al Kα radiation was generated with a voltage of 15 kV. The FTIR spectra of the modified nano-crystalline In_2O_3 were recorded with a resolution of 2 cm^{-1} by scanning 20 times from 300 to 4000 cm^{-1} at room temperature. Absorption measurements were performed using a Shimadzu UV-2100S spectrophotometer.

Photocatalytic reaction. The photocatalytic activities of In_2O_3 were examined by degrading SB with the UV irradiation of a 15 W lamp. An average irradiation intensity of 5.2 W/m^2 was maintained throughout the experiments and was measured using an internal radiometer. The aqueous dispensions of SB (100 mL, 10 ppm) and the mentioned amount of catalyst powder were placed in a Pyrex flask. The pH value of the dispensions was adjusted by adding NaOH or HNO_3 solutions. Prior to irradiation, the dispensions were magnetically stirred in the dark for 30 min to obtain an adsorption/desorption equilibrium between the dye and the surface of the catalyst in ambient air-equilibrated conditions. At specific irradiation time intervals, 5 mL of aliquot was collected and centrifuged to remove the catalyst.

RESULTS AND DISCUSSION

Characterizations of the as-prepared powders

The property of the nano-crystalline In_2O_3 surface following calcinations at various temperatures were characterized using FE-SEM. Fig. 1 shows images of the FE-SEM with a magnification of 50 000X. Fig. 1(a) shows that the surface morphology of the custom In_2O_3 was cubic and approximately 1-5 μm in size. Fig. 1(b) shows the FE-SEM images of sample S100 when part of the original cubic structure began to peel. Fig. 1(c) shows the FE-SEM images of sample S200, which had cracks at surface of the cubic structure. Fig. 1(d) shows the FE-SEM images of sample S300, which was sheet-shaped at the surface, suggesting that the dehydration of In_2O_3 caused the original cubic structure to crack in the sheet structure. Some cyclic structures were generated in the cracked sheet-shaped surface, as shown by the FE-SEM images of sample S600 (Fig. 1(g)). This structural change may have been caused by calcinations temperatures that were near the melting point of nano-crystalline In_2O_3.

Fig. 2 shows the XRD analysis of the $In(OH)_3$. The diffraction peaks of (200), (220), (013), (222), (400), (420), (422), (440), (442), and (620) of the $In(OH)_3$ appeared at 2θ = 22.26°, 31.69°, 35.55°, 39.07°, 45.43°, 51.15°, 56.45°, 66.20°, 70.79°, and 75.26°, respectively (JCPDS Card No. 85-1338). Following testing with various types of calcination temperatures, the diffraction peak had the strongest intensity when the $In(OH)_3$ (Dzhalindite) was prepared at 100 °C.[30] The XRD spectra results for the calcination temperatures ranging from 100 to 700 °C for 24 h for the In_2O_3 are shown in Fig. 2. Without calcination, the diffraction peaks of the In_2O_3 did not appear. The nano-crystalline In_2O_3 diffraction peaks of (211), (222), (400), (411), (332), (134), (440), (611), (622), (136), and (444)

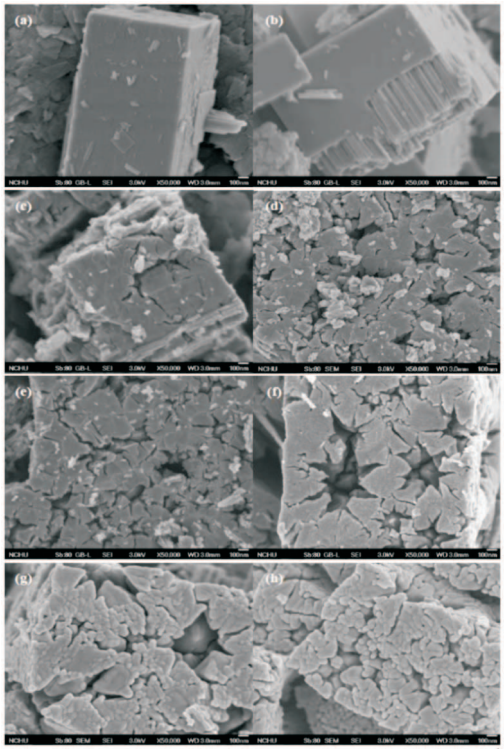

Fig. 1. SEM images of (a) commercial $In(OH)_3$; (b) commercial In_2O_3; $In(OH)_3$ are calcined at (c)100 °C, (d) 200 °C, (e) 300 °C, (f) 400 °C, (g) 500 °C, (h) 600 °C, (i) 700 °C for 24 h.

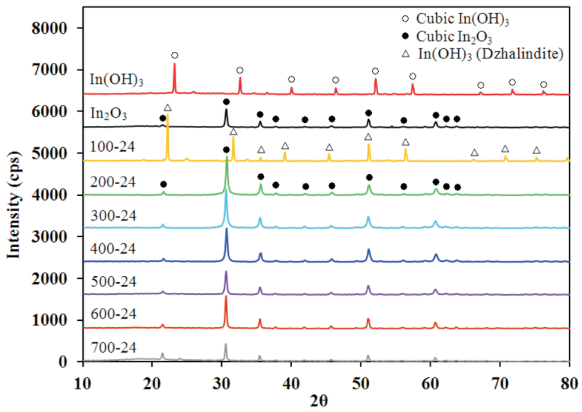

Fig. 2. XRD patterns of samples prepared with different conditions with different calcinations temperature.

were present at 2θ = 21.49°, 30.57°, 35.45°, 37.68°, 41.83°, 45.67°, 51.01°, 55.97°, 60.65°, 62.16°, and 63.65°, respectively (JCPDS Card No. 89-4595). When the calcination temperature reached 300 °C, there were strong diffraction peaks in the nano-crystalline In_2O_3. However, the intensity of the nano-crystalline In_2O_3 phase substantially decreased when the calcination temperature was 700 °C. This result is attributed to the fact that nano-crystalline In_2O_3 particles began to agglomerate and dehydrate the $In(OH)_3$, causing the original cubic structure to crack in the sheet structure. Therefore, high calcination temperatures are harmful to the formation of the nano-crystalline In_2O_3 phase. Fig. 3 shows the XRD analysis of In_2O_3 prepared by changing the calcination temperature to 300 °C for 1, 3, 6, 12, 24, and 48 h, respectively. As shown in Fig. 3, the $In(OH)_3$ phase appeared without calcinations, and the diffraction peaks of the In_2O_3 were (211), (222), (400), (411), (332), (134), (440), (611), (622), (136), and (444), as revealed at 2θ = 21.49°, 30.57°, 35.45°, 37.68°, 41.83°, 45.67°, 51.01°, 55.97°, 60.65°, 62.16°, and 63.65°, respectively, following the various calcinations times (i.e., 1, 3, 6, 12, 24, and 48 h). With the calcinations all had nano-crystalline In_2O_3 diffraction peaks, but the intensity of the diffraction peak increased with increased calcination time. However, there was a weak In_2O_3 diffraction peak following 48 h of calcination. The cracking in the original cubic structure in the sheet structure of the nano-crystalline In_2O_3 particles interfered with the weak nano-crystalline In_2O_3 diffraction peak for the calcinations time of 48 h. As a result, regardless of the calcination time, the In_2O_3 phase was achieved. The XRD results indicated that the synthesized nano-crystalline In_2O_3 sample phase was pure, which is consistent with the previous results using FE-SEM analysis.

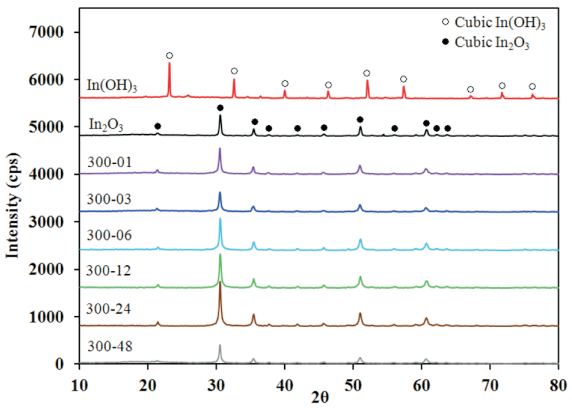

Fig. 3. XRD patterns of samples prepared with different conditions with different calcinations time.

HRXPS investigated the chemical bindings on the sample surface obtained from the calcinations of the $In(OH)_3$ at various temperatures and measured their differences. Fig. 4 shows the binding energy (BE) of the In3d and O1s from the samples following the calcinations. The custom $In(OH)_3$ and nano-crystalline In_2O_3 revealed that the

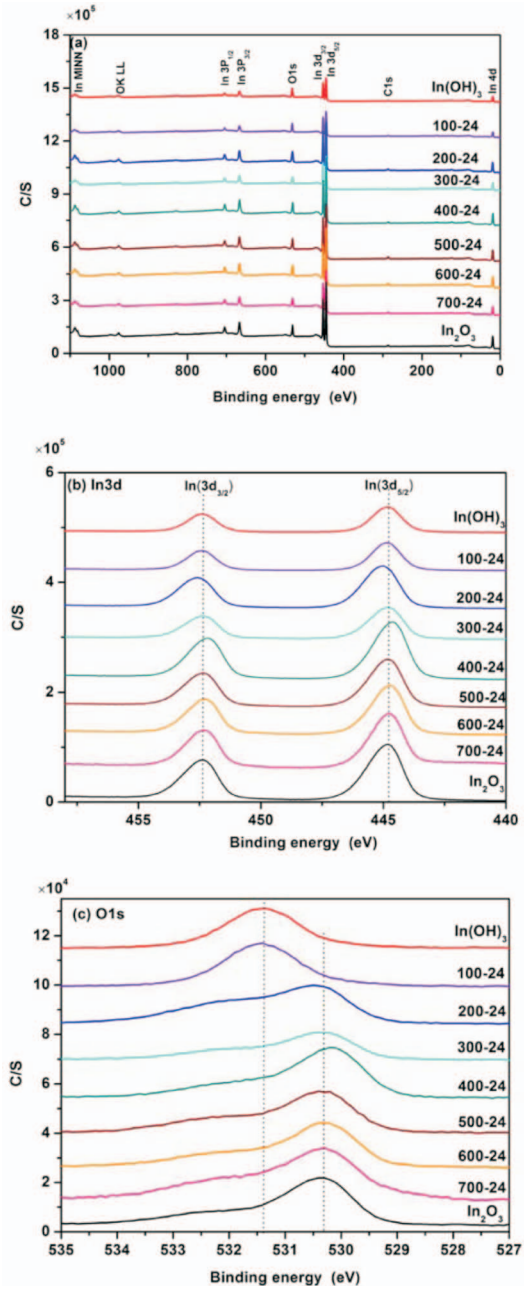

Fig. 4. The XPS spectra of $In(OH)_3$ are commercial; calcined at 100 °C, 200 °C, 300 °C 400 °C, 500 °C , 600 °C and 700 °C for 24 h; (a) Total survey; (b) In3d; (c) O 1s.

oxidation states for In^{3+} and BE(In $3d_{3/2}$) were 452.4 and 444.8 eV, respectively, meaning that the binding of O and In^{3+} for the BE(O1s) was 531.4 eV for $In(OH)_3$ and BE (O1s) = 530.3 eV for the nano-crystalline In_2O_3. Fig. 4(b) shows that the adsorptions for BE (In $3d_{3/2}$) were 452.2 to 452.6 eV and that the BE (In $3d_{5/2}$) was 444.6 to 445 eV for the oxidation state of the In^{3+} obtained from the sample through the calcinations with the $In(OH)_3$ at 100-600 °C. Fig. 4(c) shows that the spectrum of the O1s was composed of two types of chemical configurations: metal-O (530.3 eV) and metal-OH (531.4 eV).[31] The adsorption of BE was 531.4 eV for sample S100, which was consistent with the BE adsorption of 531.4 eV for the custom $In(OH)_3$, meaning they had the same configuration. Samples S200, S300, S400, S500, S600, and S700 had individual binding energies of 530.5, 530.4, 530.2, 530.4, and 530.3 eV, respectively, for the O (1s) adsorption. These were approximately the same values of the BE (O1s) for the custom nano-crystalline In_2O_3, thereby showing that the chemical configuration was In-O.

The energy change of the molecular vibration or vibration-sinning based on the $In(OH)_3$ calcinations with various temperatures were observed using an FT-IR with a range from 400 to 4000 cm^{-1} to conduct a qualitative analysis of the material. Fig. 5 shows sample S100's absorptions at 531, 780, 852, and 1160 cm^{-1} in the spectrum. The infrared spectrum of the OH group shows the characteristic absorption of the $In(OH)_3$ caused by the stretching vibration at 1160 cm^{-1} (δIn-OH),[32] and the absorption at 1100 cm^{-1} represented the bridge of the stretching vibration for the carboxylic group (δOH).[33] The absorption appeared at 1620 cm^{-1} and 3200-2600 cm^{-1}, meaning that for the stretching vibration of the H_2O (δH_2O), the absorption at 1638 cm^{-1} was the vibration of In-O, and the absorption at 3200 cm^{-1} was the vibration of the In-O-H. The vibration of In-O absorptions at 538, 564, 600, and 1638 cm^{-1} for the samples were S200, S300, S400, S500, S600, and S700.

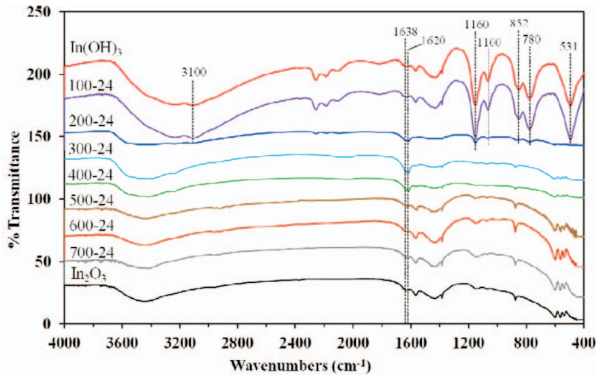

Fig. 5. FT-IR spectra of $In(OH)_3$ and In_2O_3 prepared from different calcination temperature.

The conversion process of the $In(OH)_3$ sample during the air calcination was studied using TG/differential thermal analysis (DTA), as shown in Fig. 6. The TGA curve can be divided into two weight-loss steps. The first step was between 30 and 50 °C and was attributed to the water evaporation from the $In(OH)_3$ sample. The weight loss of this step was 2%. The second step was between 186 and 277 °C and was caused by chemical dehydration. The DTA curve indicated an endothermic process in this step, and there was a weight loss of approximately 14.9%. Therefore, the nano-crystalline In_2O_3 architecture was obtained using the calcination of the as-made $In(OH)_3$ precursors.[34]

Fig. 7 shows the UV–vis absorption spectra of the nano-crystalline In_2O_3 at various calcination temperatures. The band gaps of the In_2O_3 are shown in Table 1. The differences in the band gap energies in the prepared nano-crystalline In_2O_3 were caused by the various characteristics

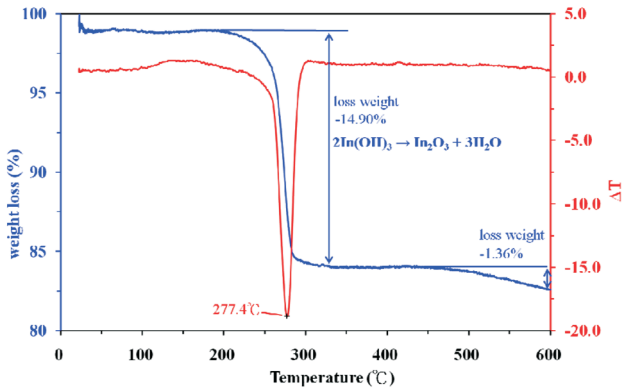

Fig. 6. TGA and DTA curves of the $In(OH)_3$.

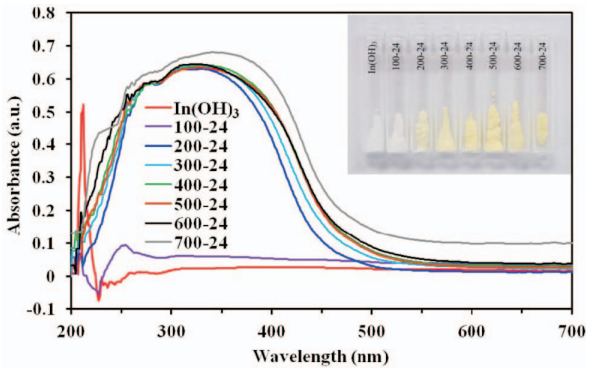

Fig. 7. UV-vis absorption spectra of the prepared In_2O_3 catalysts with different conditions with different calcinations time.

of their individual compositions. The red shift and tails of the optical absorption spectra were caused by the variations of the nano-crystalline In_2O_3 in the structures that were induced by calcination at various temperatures. In this study, the nano-crystalline In_2O_3 were in situ formed by annealing. There were oxygen vacancies at the interface of the nano-crystalline In_2O_3. The concentration of oxygen vacancy depends on calcination temperature.[35,36] Therefore, the red shift may have been caused by new energy levels in the band gap formed by the oxygen vacancy in the nano-crystalline In_2O_3. Increasing the calcination temperature for the interface interaction between the nano-crystalline In_2O_3 may induce the formation of deep oxygen vacancy energy levels in the valance band, resulting in a larger red shift in the optical band gap.

Photocatalytic Activity Evaluation

Fig. 8(a) shows the relationship between the calcination temperatures and the efficiency of degradation and that there was the same type of crystalline phase within the 200-400 °C calcination temperatures. The optimal condition for calcination was 300 °C and 24 h, and the nano-crystalline In_2O_3 had better results in the crystalline phase. In addition, Fig. 8(b) shows the calcination time for the nano-crystalline In_2O_3 for the photocatalyst producing process at 300 °C, demonstrating that this process influenced the degradation effect. The optimized results appeared at 24 h. The crystalline property of the catalyst affected the degradation results, and the crystalline phase of the nano-crystalline In_2O_3 that was calcined for 24 h was enhanced.

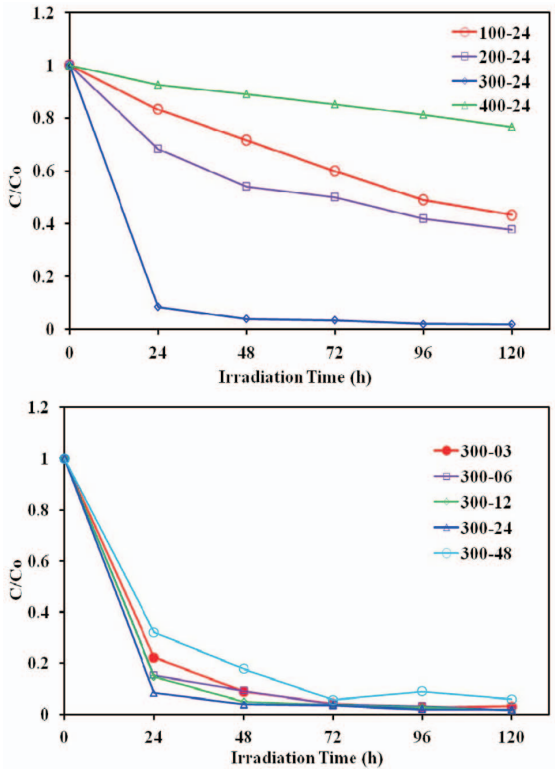

Fig. 8. Influence of (a) calcination temperature ([catalyst] = 0.5 g/L, [SB] = 10 mg/L, initial pH = 5.0, light irradiation:UV), Influence of (b) calcination time ([catalyst] = 0.5 g/L, [SB] = 10 mg/L, initial pH = 5.0, light irradiation:UV) on the SB photodegradation rate with In_2O_3.

The concentration of nano-crystalline In_2O_3 photocatalyst was related to the efficiency of the treatment system. Fig. 9 shows the reaction for 72 h with various amounts of In_2O_3 (1, 2, 3, and 4 gL^{-1}). The removal efficiency was greater than 97%. Increasing the concentration of the photocatalyst helped the adsorption of the reactant on the catalyst surface, raising the reaction efficiency of the photocatalyst.[37] Fig. 9 shows that the UV light did no affect the degradation results of the SB dye. When the amount of catalyst increased (1, 2, and 3 gL^{-1}), the degradation rate of the SB dye increased. When 4gL^{-1} of catalyst was added, the degradation rate slightly decreased, possibly because the high concentration of nano-crystalline In_2O_3 in the photocatalyst caused the over-aggregation of the particles, decreasing the activity sites at the surface and reducing the degradation rate. For the transmittance of the scattered light, adding a catalyst of 4 gL^{-1} made solution muddy and reduced the transmittance of UV light, reducing the degradation rate of the SB dye.

The band gaps of the nano-crystalline In_2O_3 catalysts following calcination at various temperatures are shown in Table 1. Table 1 shows that the band gap of sample S300 was 2.64 eV. The wavelength of the absorption light was 467.38 nm, meaning that the absorption of incident light

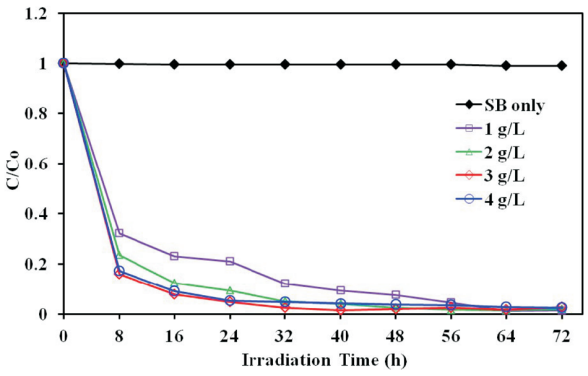

Fig. 9. Catalyst concentration effects of the SB photodegradation rate with In_2O_3.

was located within the range of visible light (400-700 nm). These two conditions are compared (i.e., ultra-violet light and visible light) in Fig. 10. The former had a 99% removal efficiency when the reaction was maintained for 144 h, and the visible light had a 98% removal efficiency in the same conditions.

Photodegradation mechanisms of SB

Photocatalytic degradation of AB1 dye yielded a number of transient organic intermediates. Temporal variations occurring in the solution of the SB dye during the degradation process with UV irradiation were examined using HPLC coupled with a PDA detector and ESI mass spectrometry. The chromatograms at pH 5 are illustrated in Fig. 11. The intermediates were identified, all with retention times of less than 50 min. We denoted the SB dye and its related intermediates as species **A-E**, **A′-B′**, **A″**, **B″**, **SA**, **SA′**, **SA″**, **a‴**, **sa, sa′-sb′**, α‴, β‴ **and** γ‴. Except for the initial SB dye (peak **A**), the other peaks initially and transformation of the intermediates. The absorption bands showed

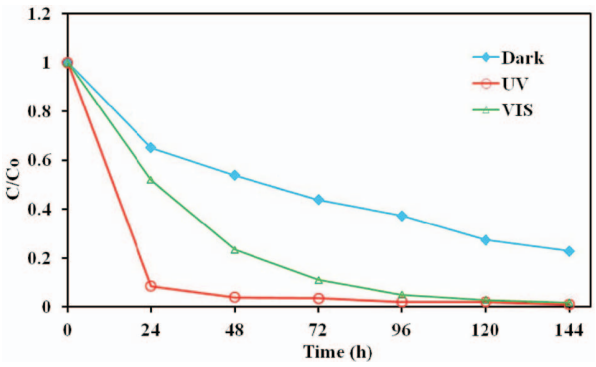

Fig. 10. Influence of visble light irradiation ([catalyst] = 0.5 g/L, [SB] = 10 mg/L, initial pH = 5.0) on the SB photodegradation rate with In_2O_3.

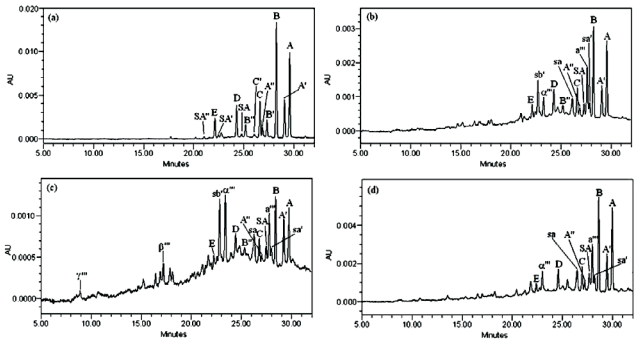

Fig. 11. HPLC/MS chromatogram of the photodegradation intermediates derived from SB. (a) 580 nm, (b) 385 nm, (c) 350 nm (d) 300 nm ([catalyst] = 1.0 g/L, [SB] = 10 mg/L, initial pH = 5.0).

that the whole conjugated chromophore structure of the SB dye, the benzophenone structure, and benzene structure might exist. The absorption spectra of each intermediate in the visible and ultraviolet spectral region are depicted in Fig. 1S. The intermediates were further identified using the HPLC-ESI mass spectrometric method, and the relevant mass spectra are illustrated in Fig. 2S. The molecular ion peaks appeared to be in the acid forms and/or basic forms of the intermediates. Results of HPLC chromatograms, UV-visible spectra, and HPLC-ESI mass spectra are summarized in Table 2. From the results of absorption and mass spectral analysis, they are identified as **A-E**, **A′-B′**, **A″**, **B″**, **SA**, **SA′**, **SA″**, **a‴**, **sa, sa′-sb′**, α‴, β‴ **and** γ‴ corresponding to the peaks **A-E**, **A′-B′**, **A″**, **B″**, **SA**, **SA′**, **SA″**, **a‴**, **sa, sa′-sb′**, α‴, β‴ **and** γ‴ in Fig. 11, respectively. Several categories of intermediates can be distinguished in Fig. 12 and Table 2. Additionally, the other peaks, designated with star marks, are depicted in Fig. 11. The absorption bands from 450 to 200 nm are observed. The concentration of these intermediates may be too low to be examined by HPLC-ESI-MS. The partial intermediates identified in the study were also identified in our previous study using Michler's ethyl ketone and ethyl violet under TiO_2/UV processes.[38,39] According to the number of the ethyl groups detached, we can characterize these intermediates. We found a pair of isomeric molecules, i.e., di-*N*-de-ethylated SB species, that differed only in their manner of loosening the ethyl groups from the benzyl groups. One of them, the **D** intermediate, was formed by the removal of an ethyl group from two different benzyl groups of the SB molecule.

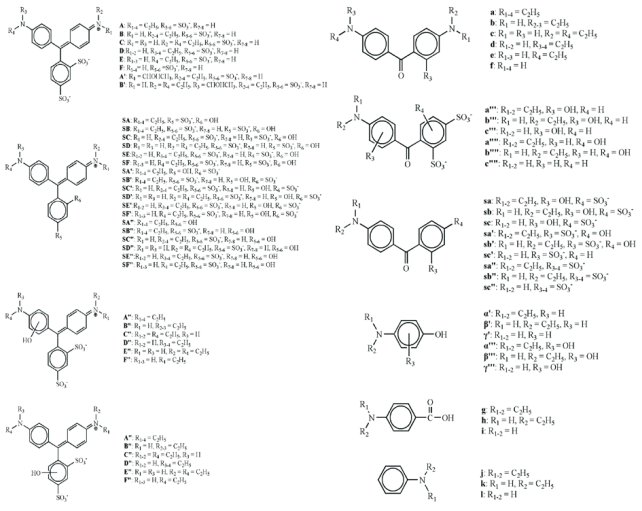

Fig. 12. Chemical structure of photodecomposed intermediates.

Table 2. Summary of the SB photocatalytic degradation inter-mediates identified by the HPLC-PDA-ESI/MS

Intermediates	Retention Time (min)	$[M + H^+]/[M - H^+]$ (m/z) [a]	Characteristic Absorption (nm)
A	29.699	545.11/543.10	637.1, 412.6, 313.1
B	28.296	517.10/515.09	622.4, 403.0, 310.7
C	26.585	489.03/487.28	607.7, 395.7, 305.9
D	24.164	489.09/487.21	607.7, 369.9, 302.4
E	21.832	461.02/459.20	591.8, 388.5, 302.4
A′	26.892	561.10/559.15	647.0, 412.6, 313.1
B′	25.178	533.27/531.14	627.3, 413.8, 309.5
A″	26.153	561.22/559.00	637.1, 411.4, 310.7
B″	24.722	533.15/531.34	623.6, 389.7, 317.9
SA	28.103	481.54/479.52	621.2, 401.7, 310.7
SA′	22.223	481.22/479.26	611.4, 393.3, 308.3
SA″	17.682	481.44/479.21	607.7, 311.9
a‴	24.647	430.27/428.24	435.6, 295.2
sa	27.831	350.08/348.51	436.9, 298.8
sa′	27.996	350.23/348.32	457.5, 275.0
sb′	22.882	322.33/320.16	419.9, 266.6
α‴	23.439	182.20	362.1
β‴	17.139	154.14	350.2
γ‴	8.572	126.07	332.2

Loosening two methyl groups from the same benzyl group of the SB dye produced the other one, **C** intermediate. Therefore, considering the polarity of the **C** intermediates is greater than that of the **D** intermediate, we expected the latter to be eluted after the **C** intermediate. Also, to the extent that two *N*-ethyl groups are stronger auxochromic moieties than the *N*,*N*-diethyl or amino groups are, the maximal wavelengths shorter than the band position of the **D** intermediate. There is a similar situation in the other intermediates category. **A**-**E** intermediates may be the *N*-de-ethylation of the SB dye.

This result suggests that the removal of SB was *N-de-ethylation* in a stepwise manner (i.e., ethylation groups were removed one by one, as confirmed by the gradual peak wavelength shifts). Therefore, *N-de-ethylation* might be the dominating mechanism for the removal of SB by the In_2O_3 process. The cleavage of the SB chromophore ring structure is not the significant step. Based on these experimental results, reaction pathways for the *N-de-ethylation* of SB are proposed and depicted in Fig. 13. According to earlier reports.[40] The intermediates may be the N-de-ethylation of a, produced by symmetric cleavage of the SB chromophore ring structure (Fig. 13). According to earlier reports,[14,41] most oxidative Ndealkylation processes (pathway I) are preceded by the formation of a nitrogen-centered radical and destruction of dye chromophore structures (pathway II) is preceded by the generation of a carbon-centered radical. ·OH radical attacked the diethylaminobenzene (or disulfonylbenzene) ring of the SB chromophore structure (pathway III-IV) and substituted the sulfonyl group (pathway V) intermediates, which were found for the first time in In_2O_3 photocatalysis process. Consistent with

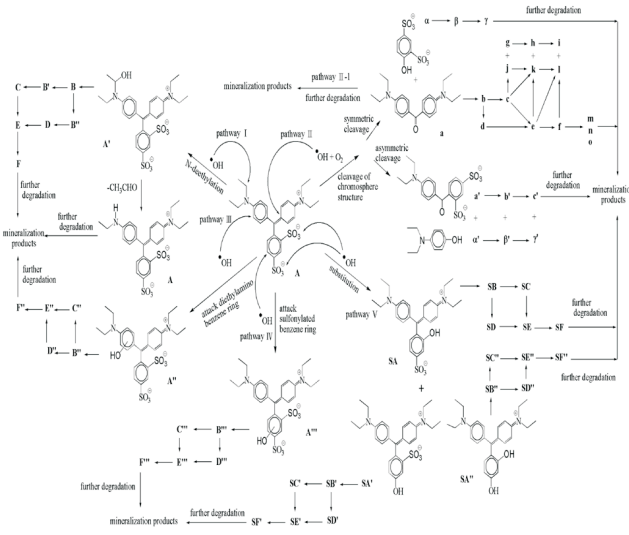

Fig. 13. Proposed photocatalytic degradation mechanism of the SB with In_2O_3.

these, degradation of SB must occur via the five different photodegradation pathways listed in Fig. 13. To be consistent with the above statement, the degradation of SB must occur via two different photooxidation pathways (destruction of the chromophore structure and *N-deethylation*) due to the formation of the different radicals (either carbon-centered radical or nitrogen-centered radical). There is no doubt that electron injection from the dye to the positive holes of In_2O_3 yields the dye cationic radical. After this stage the cationic radical Dye^{+} can undergo hydrolysis and/or deprotonation pathways of the dye cationic radicals, which in turn are determined by the different adsorption modes of SB on the In_2O_3 particle surface.

CONCLUSIONS

A nano-crystalline In_2O_3 was synthesized using the calcinations method and by meticulously controlling the synthesis parameters. The photocatalytic efficiencies of the powder suspensions were evaluated by measuring the SB concentration. The optical calcinations synthesis parameters for the nano-crystalline In_2O_3 photocatalysts were found to be calcinations at 300 ^{o}C for 24 h under UV irradiation and visible light irradiation. In addition, the optimal calcination condition of 300 ^{o}C for 24 h provided enhanced results for the crystalline phase. The calcination temperature of the photocatalyst producing process influences the degradation effect. Nano-crystalline In_2O_3 are a promising form of visible light-responsive photocatalyst. The reaction mechanisms of SB were proposed and discussed in this research. *N-deethylation* might be the main reaction pathway for the removal of SB from aqueous solutions.

ACKNOWLEDGMENT

This research was supported by the National Science Council of the Republic of China (NSC 99-2113-M-142-001-MY2).

REFERENCES

1. Azmi, W.; Sani, R. K. *Enzyme. Microb. Tech*. **1998**, *22*, 185.
2. An, H.; Qian, Y.; Gu, X. H.; Tang, W. Z. *Chemosphere* **1996**, *33*, 2533.
3. Walker, G. M.; Weatherley, L. R. *Water Res.* **1997**, *31*, 2093.
4. Namasivayam, C.; Arasi, D. J. S. E. *Chemosphere* **1997**, *34*, 401.
5. Wang, J.-M.; Huang, C.-P.; Cha, O.-K.; Kim, D.-W. J. *Colloid Interf. Sci.* **1998**, *208*, 518.
6. Mittal, A.; Gajbe, V. J. M. *J. Hazard. Mater*. **2008**, *150*, 364.
7. Lee, W.-L.; Lin, J.-H.; Chang, J.-L.; Chen, J.-Y.; Cheng, M. C.; Chen, C. C. *J. Mol. Catal. A: Chem* **2012**, *361-362*, 80.
8. Chen, S.-F.; Yu, X.-L.; Zhang, H.-Y.; Liu, W. *J. Hazard. Mater.* **2010**, *180*, 735.
9. Liu, G.-D. *Int. J. Electrochem. Sci.* **2011**, *6*, 2162.
10. Baptista, M. S.; Indig, G. L. *J. Phys. Chem. B* **1998**, *102*, 4678.
11. Carey, J. H.; Lawrence, J.; Tosine, H. M. B. *Environ. Contam. Tox*. **1976**, *16*, 697.
12. Steven, N. F.; Allen J. B. *J. Phys. Chem.* **1977**, *81*, 1484.
13. Fan, H.-J.; Liu, C.-S.; Lee, W.-L.; Chiou, M.-R.; Chen, C.-C. *J. Hazard. Mater.* **2011**, *185*, 227.
14. Chen, C.-C.; Lu, C.-S. *Environ. Sci. Technol.* **2007**, *41*, 4389.
15. Tang, J. W.; Durrant, J. R.; Klug, D. R. *J. Am. Chem. Soc.* **2008**, *130*, 13885.
16. Zhou, Z.-B.; Cui, R.-Q.; Pang, Q.-J.; Wang, Y. D.; Meng, F.-Y.; Sun, T. T.; Ding, Z.-M.; Yu, X. B. *Appl. Surf. Sci.* **2001**, *172*, 245.
17. Liang, Y.-X.; Li, S.-Q.; Nie, L.; Wang, Y.-G.; Wang, T.-H. *Appl. Phys. Lett.* **2006**, *88*, 193119.
18. Kim, D.-W.; Hwang, I.-S.; Kwon, S.-J.; Kang, H.-Y.; Park, K. S.; Choi, Y.-J.; Choi, K.; Park, J. G. *Nano Lett.* **2007**, *7*, 3041.
19. Curreli, M.; Li, C.; Sun, Y.; Lei, B. *J. Am. Chem. Soc.* **2005**, *127*, 6922.
20. Bianchi, S.; Comini, E.; Ferroni, M.; Faglia, G.; Vomiero, A.; Sberveglieri, G. *Sens. Actuat. B: Chem.* **2006**, *118*, 204.
21. Kuo, C.-Y.; Lu, S.-Y.; Wei, T. Y. J. *Cryst. Growth* **2005**, *285*, 400.
22. Li, B.; Xie, Y.; Jing, M.; Rong, G.; Tang, Y.; Zhang, G. *Langmuir* **2006**, *22*, 9380.
23. Gurlo, A.; Ivanovskaya, M.; Barsan, N.; Schweizer-Berberich, M.; Weimar, U.; Gopel, W.; Die' guez, A. *Sens. Actuat.* **1997**, *44*, 327.
24. Soulantica, K.; Erades, L.; Sauvan, M.; Senooq, F.; Maisonnat, A.; Chandret, B. *Adv. Funct. Mater.* **2003**, *13*, 553.
25. Zhang, D.-H.; Li, C.; Han, S.; Liu, X.-L.; Tang, T.; Jin, W.; Zhou, C.-W. *Appl. Phys. Lett.* **2003**, *82*, 112.
26. Benamar, E.; Rami, M.; Messaoudi, C.; Sayah, D.; Ennaoui, A. *Sol. Energy Mater. Sol. Cells* **1999**, *56*, 125-139.
27. Odaka, H.; Shigesato, Y.; Murakami, T.; Iwata, S. *Jpn. J. Appl. Phys.* **2001**, *40*, 3231.
28. Lu, X.-F.; Zhang, L.; Zhao, H.; Yan, K.; Cao, Y.; Meng, L.-M. *J. Mate. Sci. Technol.* **2012**, *28*, 396.
29. Yu, C.-X.; Zhang, H.; Liu, W. *Langmuir* **2010**, *26*, 14814.
30. Yan, T.-J.; Wang, X.-X.; Long, J.-L.; Lin, H.-X.; Yuan, R.-H.; Dai, W.-X.; Li, Z.-H.; Fu, X.-Z. *New J. Chem.* **2008**, *32*, 1843.
31. Zhu, H.; Wang, X.-L.; Wang, Z.-G.; Yang, C.; Yang, F.; Yang, X.-R. *J. Phys. Chem. C* **2008**, *112*, 15285.
32. Tzu, T. T.; Wenjea, J. T. *Ceram. Int.* **2009**, *35*, 2837.
33. Poznyak, S. K.; Kulak, A. I. *Electrochim. Acta* **2000**, *45*,

1595.
34. Tao, X. J.; Sun, L.; Li, F. Z. W. *Nanoscale Res. Lett.* **2010**, *5*, 383.
35. Zheng, M.-J.; Zhang, L.-D.; Zhang, X.-Y.; Zhang, J.; Li, G.-G. *Chem. Phys. Lett.* **2011**, *334*, 298.
36. Sun, H.-G.; Fan, W.-L.; Li, Y.-L.; Chen, X.; Li, P.; Zhao, X. *J. Phys. Chem. C* **2010**, *114*, 3028.
37. Chen, C.-C.; Lu, C.-S. *J. Phys. Chem. C* **2007**, *111*, 13922.
38. Lu, C.-S.; Chen, C.-C.; Mai, F.-D.; Wu, Y.-C. *J. Photochem. Photobiol., A* **2007**, *187*, 167-176.
39. Chen, C.-C.; Fan, H.-J.; Lu, C.-S.; Jang, C.-Y.; Jan, J.-L.; Lin, H.-D. *J. Photochem. Photobiol., A* **2006**, *184*, 147.
40. Laude, B. L.; Asirvatham, M. R.; Mann, C. K. *J. Org. Chem.* **1977**, *42*, 670.
41. Chen, C.-C.; Lu, C.-S.; Mai, F.-D,; Weng, C. S. *J. Hazard. Mater.* **2006**, *137*, 1600.

